

Current-induced switching of a van der Waals ferromagnet at room temperature

Received: 9 July 2023

Accepted: 30 January 2024

Published online: 19 February 2024

Shivam N. Kajale^{1,4}, Thanh Nguyen^{2,4}, Corson A. Chao³, David C. Bono³, Artittaya Boonkird², Mingda Li² & Deblina Sarkar¹✉

Recent discovery of emergent magnetism in van der Waals magnetic materials (vdWMM) has broadened the material space for developing spintronic devices for energy-efficient computation. While there has been appreciable progress in vdWMM discovery, a solution for non-volatile, deterministic switching of vdWMMs at room temperature has been missing, limiting the prospects of their adoption into commercial spintronic devices. Here, we report the first demonstration of current-controlled non-volatile, deterministic magnetization switching in a vdW magnetic material at room temperature. We have achieved spin-orbit torque (SOT) switching of the PMA vdW ferromagnet Fe_3GaTe_2 using a Pt spin-Hall layer up to 320 K, with a threshold switching current density as low as $J_{\text{sw}} = 1.69 \times 10^6 \text{ A cm}^{-2}$ at room temperature. We have also quantitatively estimated the anti-damping-like SOT efficiency of our $\text{Fe}_3\text{GaTe}_2/\text{Pt}$ bilayer system to be $\xi_{\text{DL}} = 0.093$, using the second harmonic Hall voltage measurement technique. These results mark a crucial step in making vdW magnetic materials a viable choice for the development of scalable, energy-efficient spintronic devices.

Magnetic materials-based spintronic devices^{1–3} hold great promise as energy-efficient, non-volatile memories and building blocks of neuromorphic⁴ and probabilistic^{5,6} computing hardware. However, just a few optimal material systems, like CoFeB/MgO^{7–9} in particular, have been identified for scalable device applications over the last two decades. The discovery of emergent magnetism in two-dimensional van der Waals (vdW) magnetic materials^{10–13} has opened a new arena for material exploration for spintronic technologies¹⁴. vdW magnetic materials provide scalable, perpendicular magnetic anisotropy (PMA) alternatives to CoFeB/MgO while also providing atomically smooth interfaces down to monolayer thicknesses to help maintain device performance. However, a crucial requirement for the development of spintronic devices with vdW materials is the deterministic switching of PMA magnetism using current or voltage drives at room temperature.

The Fe_nGeTe_2 family of metallic ferromagnets^{12,15,16} has shown favorable signs for technological translation in recent years, with Curie temperature reaching close to room temperature,

while also exhibiting a strong PMA^{12,15}. Several reports on the current-control of PMA magnetization in Fe_3GeTe_2 have appeared, in spin-orbit torque (SOT) systems utilizing heavy metals^{17,18}, topological insulators¹⁹ and topological semimetals^{20–22}. However, these reports are limited to operation only at cryogenic temperatures (up to 200 K). The recently reported vdW ferromagnet, Fe_3GaTe_2 (FGaT), which is a close analogue of Fe_3GeTe_2 , holds promise in this regard²³. It is a metallic ferromagnet, with Curie temperature exceeding 350 K and a strong perpendicular magnetic anisotropy up to $3.88 \times 10^5 \text{ J m}^{-3}$, making it suitable for developing scalable and stable magnetic tunnel junctions²³. In fact, FGaT based magnetic tunnel junctions (and spin-valves in general) have already been reported^{24–27}, with an impressive tunneling magneto-resistance (TMR) ratio up to 85% at 300 K observed in the FGaT/WSe₂/FGaT system²⁴. This makes FGaT a favorable candidate for exploring room temperature current-based control of PMA magnetization in vdW material systems.

¹MIT Media Lab, Massachusetts Institute of Technology, Cambridge, MA, USA. ²Department of Nuclear Science and Engineering, Massachusetts Institute of Technology, Cambridge, MA, USA. ³Department of Materials Science and Engineering, Massachusetts Institute of Technology, Cambridge, MA, USA. ⁴These authors contributed equally: Shivam N. Kajale, Thanh Nguyen. ✉e-mail: deblina@mit.edu

Here, we report the non-volatile, deterministic magnetization switching at room temperature of the vdW ferromagnet using $\text{Fe}_3\text{GaTe}_2/\text{Pt}$ bilayer devices. Bulk crystals of Fe_3GaTe_2 were grown using a self-flux method, and its magnetic properties were studied in the bulk and in exfoliated sheets. Bilayer devices of multi-layer FGaT and 6 nm Pt were fabricated to demonstrate type-z spin-orbit torque switching^{28,29} of FGaT magnetization up to 320 K in the presence of a 100 Oe in-plane magnetic field, with a threshold current density of $1.69 \times 10^6 \text{ A cm}^{-2}$. Furthermore, second harmonic Hall voltage measurements were used to estimate the anti-damping-like field component which is responsible for the current-induced switching, and the SOT efficiency of the FGaT/Pt system.

Results

Growth and characterization of Fe_3GaTe_2

We first present our characterization of bulk crystalline vdW FGaT synthesized using a Te self-flux method (see Methods). The FGaT unit cell possesses a hexagonal symmetry with space group $\text{P6}_3/\text{mmc}$ (no. 194), like that of isostructural Fe_3GeTe_2 , wherein two adjacent quintuple layer substructures with two inequivalent Fe crystallographic sites form a vdW gap between the tellurium layers (Fig. 1a). Millimeter-sized hexagonal planar crystals were measured with powder X-ray diffraction and showcase prominent (00L) Bragg peaks which were analyzed using a Rietveld refinement (Fig. 1b). To verify the composition of our crystals, we performed energy-dispersive X-ray

spectroscopy elemental mapping on a diverse set of bulk crystals and exfoliated flakes which all exhibited the correct atomic ratio (Fig. 1c). Hysteresis loops of the direct current magnetization on bulk FGaT were performed from 3 K to 400 K with a magnetic field applied out-of-plane (OOP) as shown in Fig. 1d. Both the coercive field and the saturation magnetization gradually decrease with increasing temperature up to the transition temperature near 340 K. These are complemented by measurements of the Hall resistivity with magnetic field applied out-of-plane which showcase a prominent anomalous Hall effect (AHE) accompanying the magnetization up to the same temperature (Fig. 1e) with a room temperature Hall angle of 2.6° . The temperature dependence of magnetization with an applied out-of-plane magnetic field of 1000 Oe under field-cooling shows a departure near the Curie temperature from the zero-field-cooling situation (Fig. 1f). The heat capacity manifests a prominent peak (Fig. 1g) and the temperature-dependent longitudinal resistivity displays a noticeable change of slope (Fig. 1h) both near 340 K. Altogether, these complementary measurements consistently indicate room-temperature magnetic properties and the high ferromagnetic transition temperature of the bulk FGaT crystals.

Next, we have characterized magnetism in exfoliated nanosheets of FGaT using a combination of AHE and polar magneto-optical Kerr effect (MOKE) measurements. Figure 2a shows the temperature dependent AHE hysteresis loops for OOP field sweep for a 29 nm thick FGaT flake. As depicted in the schematic (Fig. 2a inset), current is

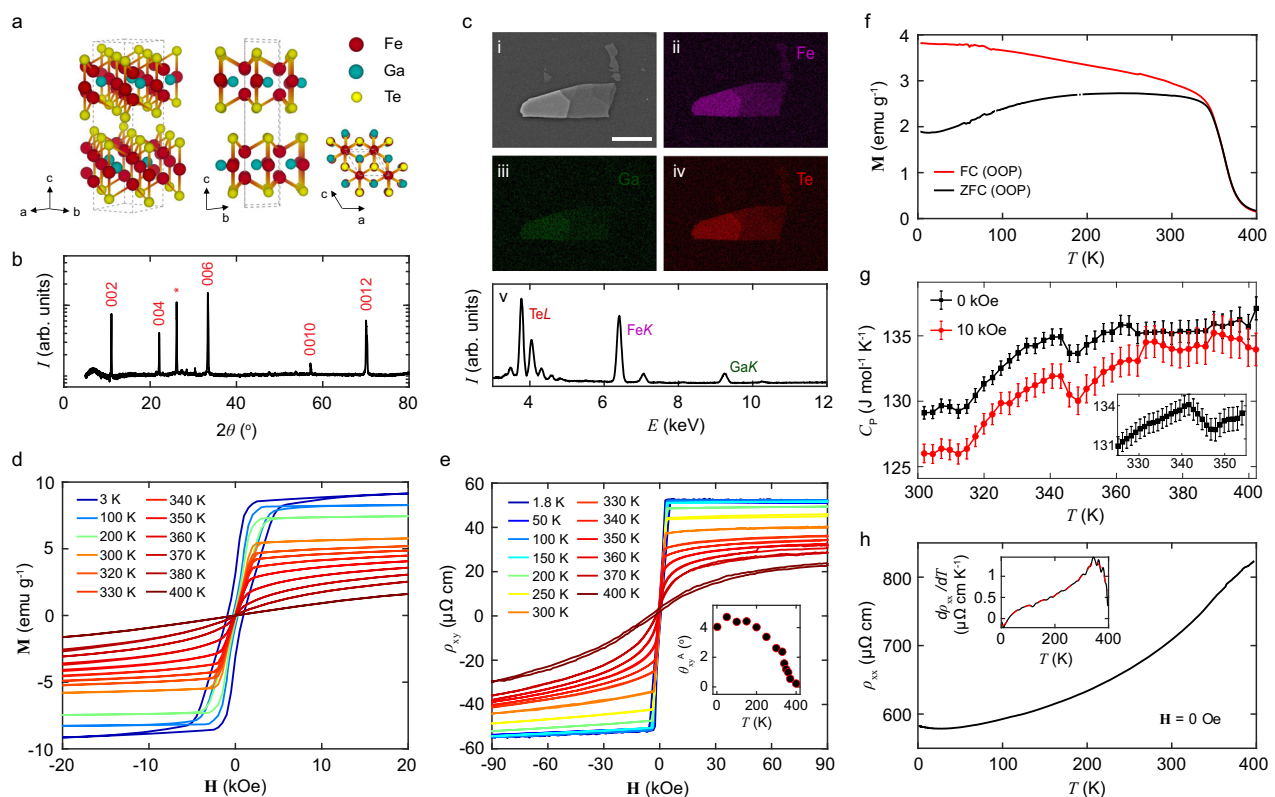


Fig. 1 | Characterization of Fe_3GaTe_2 bulk crystals. **a** Crystal structure of Fe_3GaTe_2 under different orientations: general view, bc -plane and ac -plane. **b** Powder x-ray diffraction (PXRD) pattern of the bulk crystal with indexed prominent Bragg peaks. **c** Scanning electron microscope image of an exfoliated flake on SiO_2/Si substrate (i) with corresponding elemental Fe (ii), Ga (iii) and Te (iv) maps and energy-dispersive spectra (v). The scale bar on the SEM image is $20 \mu\text{m}$. **d** Spontaneous magnetization dependence with magnetic field applied out-of-plane at different temperatures. **e** Hall resistivity of a bulk sample measured at different temperatures with the magnetic field applied in the out-of-plane direction. Inset shows the measured anomalous Hall angle as a function of temperature.

f Spontaneous magnetization under field-cooled (FC) and zero-field-cooled (ZFC) conditions with respect to temperature with the magnetic field (1000 Oe) applied out-of-plane. **g** Specific heat capacity measurement with zero and a 10 kOe magnetic field applied in the out-of-plane direction. Inset shows a fine scan at zero field near the magnetic transition showing a small upturn near the magnetic transition temperature. Error bars represent the standard deviation. **h** Temperature dependence of the bulk longitudinal resistivity. Inset shows the derivative of the longitudinal resistivity with respect to temperature. A broad peak indicates the presence of a magnetic transition.

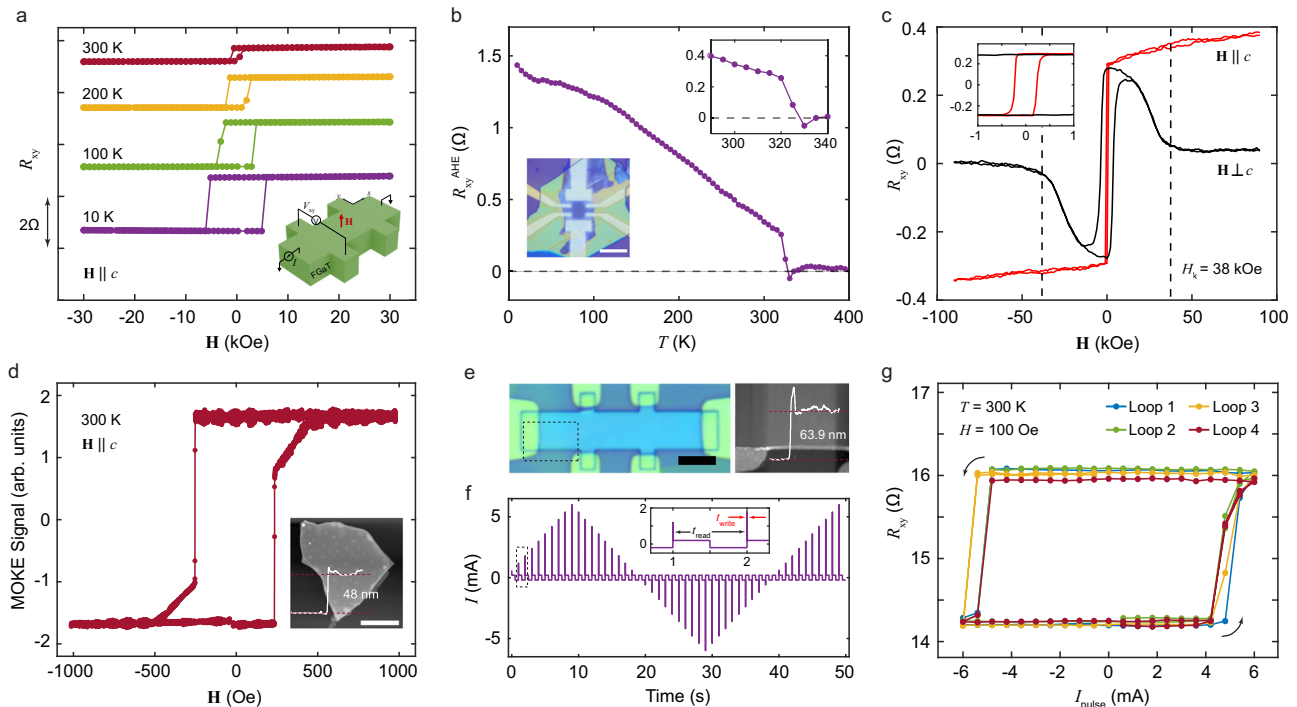


Fig. 2 | Magneto-transport in exfoliated FGaT and switching of FGaT/Pt devices.

a Temperature dependent hysteresis plots of the device for out-of-plane field sweeps ($\mathbf{H} \parallel c$). Data offset along y -axis for clarity. Inset: Schematic of measurement geometry. **b** Variation of anomalous Hall resistance of a (29 nm) FGaT flake against temperature, indicating a Curie temperature of ≈ 328 K. Insets – optical image of the FGaT Hall bar on bottom left, zoomed in view of $R_{xy}^{AHE} - T$ close to the Curie temperature. **c** Comparison of room temperature Hall resistance curves of the FGaT device for field swept OOP ($\mathbf{H} \parallel c$) and in-plane ($\mathbf{H} \perp c$), with anisotropy field

of $H_k = 38$ kOe denoted by vertical dashed lines. Inset: Low field zoom-in view of the plots. **d** Room temperature polar MOKE curve of a (48 nm) FGaT flake, indicative of strong PMA and a coercivity $H_c = 235$ Oe. **e** Optical image of the FGaT (57.9 nm)/Pt (6 nm) device (left) and its AFM micrograph (right). **f** Current sequence applied to the FGaT/Pt device for magnetization switching experiments, with the inset clarifying the nature of write pulses (t_{write}) and read pulses (t_{read}). **g** Cyclic magnetization switching curves observed for the FGaT/Pt devices over four consecutive current pulsing loops, at 300 K under in-plane bias field of 100 Oe. Scale bars: 5 μm .

applied along the x – axis and the transverse voltage (V_{xy}) is measured along y – axis for the AHE measurements. The hysteresis loops exhibit a rectangular nature right up to room temperature, indicating a strong perpendicular magnetic anisotropy. Figure 2b shows the temperature dependence of remanent anomalous Hall resistance. The R_{xy}^{AHE} plotted here is the difference in transverse resistance of the device, recorded while warming up the device at zero magnetic field, after cooling under +3 T and –3 T out-of-plane field, respectively. The sharp drop in R_{xy}^{AHE} above 320 K (inset of Fig. 2b) marks the transition from ferromagnetic to paramagnetic state with a Curie temperature $T_C \approx 328$ K, slightly lower than the bulk value. The material exhibits an effective anisotropy field of $H_k = 38$ kOe at 300 K as evident from the R_{xy} plot for near in-plane magnetic field sweeps ($\mathbf{H} \perp c$) in Fig. 2c. The inset provides R_{xy} vs \mathbf{H} with finer field steps indicating a room temperature coercivity of 220 Oe for the OOP field sweep. To further confirm room temperature magnetic properties of the FGaT flakes, we report polar MOKE measurement of a 48 nm-thick flake in Fig. 2d. The hysteresis plot shows a near 100% remanence confirming the presence of strong PMA, with a coercivity of 235 Oe. The two-step nature of the hysteresis loop can be attributed to presence of multi-domains in the relatively thick flake, as previously reported³⁰. We would like to note that the MOKE plots correspond to a flake exposed directly to air for more than a week, indicative of the lack of material degradation (barring surface oxidation which cannot directly be concluded from MOKE) and hence, the air-stability of FGaT nanosheets.

Deterministic switching of vdW magnet

To demonstrate current induced switching of magnetism in FGaT, we have fabricated bilayer devices of exfoliated FGaT flakes (bottom) and 6 nm sputtered Pt (top). The bilayer stack is patterned into a Hall bar

device and anomalous Hall resistance measurements are used to track the magnetization state of FGaT in the switching experiments. Figure 2e shows the optical image of one such device, D1, with 57.9 nm FGaT and 6 nm Pt patterned into a 5 μm wide Hall bar. The device is subjected to a current waveform as shown in Fig. 2f, with 1 ms write pulses up to a maximum of 6 mA, at 1 s intervals, with R_{xy} being recorded after each current pulse. Figure 2g shows the Hall resistance across this device for the cyclic current sweeps. The measurements are performed at 300 K in the presence of a 100 Oe in-plane magnetic field applied parallel to current direction. The device transitions from a low resistance to a high resistance state and vice versa, for a current pulse of ± 5.4 mA, indicating 180° switching of the OOP magnetization, with appreciable repeatability across four consecutive measurement cycles. This corresponds to a threshold switching current density of 1.69×10^6 A cm^{-2} , which compares well with previous reports of ferromagnet/Pt systems (Supplementary Information Section 3). The small asymmetry in the positive and negative current switching cycles can be attributed to an OOP component of external magnetic field acting on the device due to slight misalignment between the field direction and the true sample plane. We have observed similar current-induced switching behavior in three more of our FGaT/Pt devices (viz. D2, D3, D4) as documented in Section 2 of the Supplementary Information.

As depicted in Fig. 3a, a charge current I_c injected in the plane of the device results in the creation of a transverse spin-current in the Pt layer due to spin-Hall effect. The vertically flowing component of the spin current results in an in-plane oriented spin accumulation at the FGaT/Pt interface. The in-plane damping-like torque applied by the moment of these spins drives the magnetization in-plane while the current pulse is active. The torque from the accompanying external in-plane field, parallel to current direction, favors relaxation of the

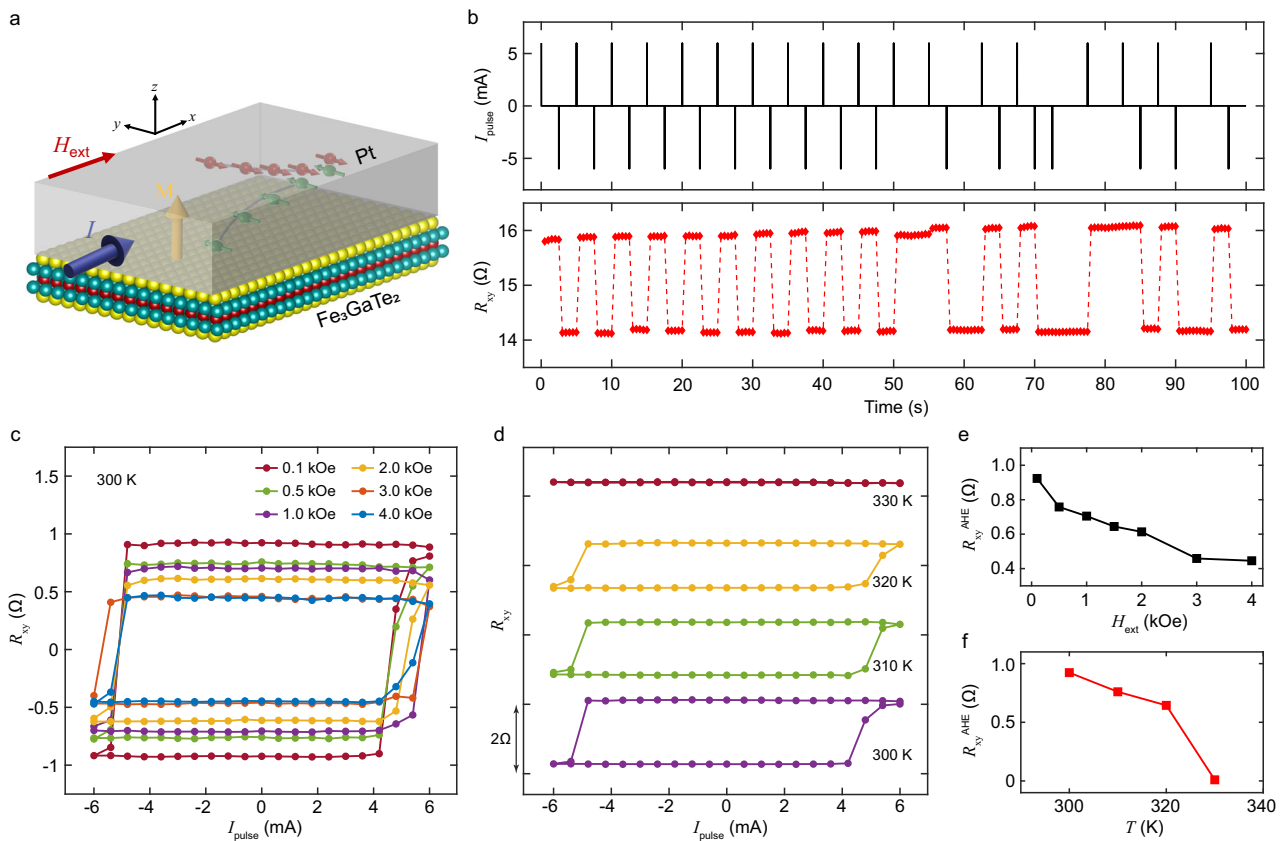


Fig. 3 | Robust current-driven switching and its field and temperature dependence. **a** Schematic diagram showing generation of spin-current in Pt layer in response to a planar current injection (I) due to spin-Hall effect. Vertical component of the in-plane polarized spin-current is incident at the Pt/FGaT interface, resulting in spin accumulation and spin-orbit torque on FGaT magnetization \mathbf{M} . **b** Deterministic, non-volatile switching of FGaT magnetization by a train of current

pulses, 1 ms wide and ± 6 mA in magnitude. Modulation of current-induced R_{xy} hysteresis curves upon variation of **c** externally applied in-plane magnetic field magnitude and **d** temperature of the system. Data offset along y-axis for clarity. **e, f** Variation of anomalous Hall resistance against in-plane field **e** and system temperature **f**.

magnetization to one of the two OOP directions (opposite for positive and negative current) after the current pulse is removed³¹, resulting in deterministic, non-volatile switching of magnetization in the PMA material. Figure 3b shows the robust control of magnetization state in device D1 at room temperature using a train of random current pulses, 1 ms wide and ± 6 mA in magnitude. We further studied the dependence of magnetization switching curves for varying in-plane field and increasing temperature. In Fig. 3c, we observe that increasing the magnitude of applied in-plane magnetic field results in vertical shrinking of the switching curves. Increasing in-plane magnetic field drives the steady state magnetization of FGaT further away from the c-axis, decreasing the OOP magnetization component. Thus, we can expect a reduction in the anomalous Hall resistance of the device ($\propto M_z$) on increasing the in-plane magnetic field, in agreement with our observations (Fig. 3e). Similar trend is also observed in D2 (Supplementary Fig. 3). We also report the response of device D2 to current pulsing, for field variation in other principal axes, i.e., out-of-plane and in-plane (orthogonal to current) in Supplementary Fig. 4, where deterministic switching is not observed. Similarly, we have found that the AHE splitting of the switching curves decreases on increasing the temperature above 300 K (Fig. 3d). We continue to see a sharp transition in resistance up to 320 K, but at 330 K, there is no clear change in R_{xy} across the current cycle. Once again, this agrees well with the expectation that the magnitude of magnetization decreases with increasing temperature and goes to zero beyond the Curie temperature (≈ 328 K). In fact, the trend of R_{xy}^{AHE} observed for these current pulse sweeps (Fig. 3f) matches well with the R_{xy}^{AHE} vs T observed in our FGaT-only devices (Fig. 2b). Similar measurements performed on

device D2, over a boarder temperature range and with finer sampling close to the switching current shows a gradual decrease in threshold switching current with increasing temperature, as is expected due to decrease in magneto-crystalline anisotropy and coercivity at higher temperatures (Supplementary Fig. 3).

Estimation of Spin-Orbit Torque efficiency

To quantify the spin-orbit torque in our FGaT/Pt bilayer system, we have performed second harmonic Hall (SHH) voltage measurements^{32,33}. As depicted in Fig. 4a, the SHH voltage ($V_{xy}^{2\omega}$) is measured along the y - axis for an ac current excitation along the x - axis, in presence of an externally applied in-plane magnetic field, H_{ext} , of varying magnitude and azimuthal angle ϕ with respect to the x - axis. For an arbitrary orientation of magnetization, with polar angle θ_m and azimuthal angle ϕ_m , the transverse resistance contains contributions from the anomalous Hall effect and the planar Hall effect,

$$R_{xy}^{\omega} = R_{xy}^{\text{AHE}} \cos \theta_m + R_{xy}^{\text{PHE}} \sin^2 \theta_m \sin(2\phi_m) \quad (1)$$

where, R_{xy}^{AHE} and R_{xy}^{PHE} are the anomalous Hall resistance and planar Hall resistance of the device, respectively. Upon injecting an AC current into the device, the current induced field-like and anti-damping-like torques drive periodic oscillations of magnetization about its equilibrium position, resulting in harmonic oscillation of the transverse resistance R_{xy}^{ω} . Thus, the recorded transverse voltage $V_{xy}(t) = I_{\text{ac}}(t)R_{xy}(t)$ contains a 2ω component which can be detected through lock-in measurement. However, the SHH voltage also has contributions from thermal effects which appear in addition to the

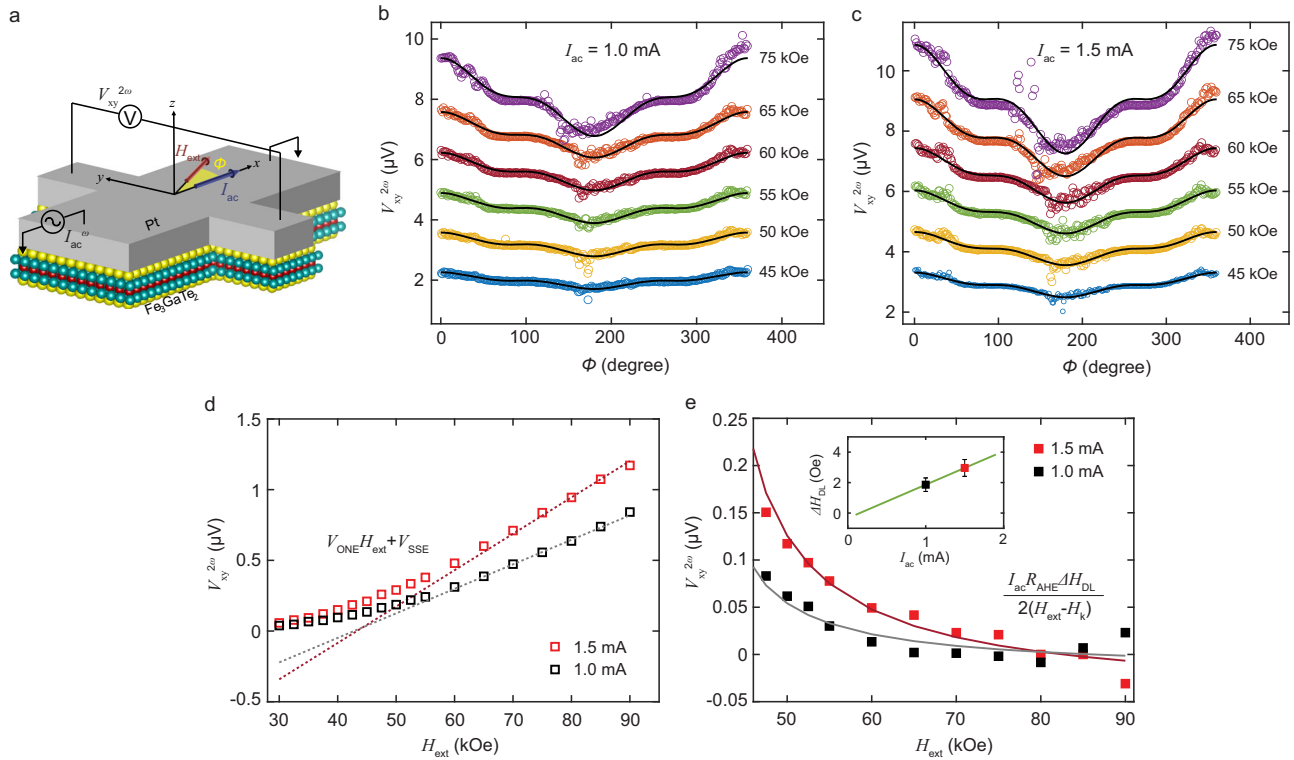


Fig. 4 | Second harmonic Hall resistance and estimation of SOT efficiency.

a Schematic illustration of the second harmonic Hall (SHH) voltage measurement. External field H_{ext} is applied in the sample (xy -) plane at an angle ϕ from x -axis. Current is applied along x -axis and SHH voltage ($V_{xy}^{2\omega}$) is measured along the y -axis. **b, c** $V_{xy}^{2\omega}$ measured for in-plane magnetic field rotation for (b) $I_{ac} = 1$ mA and (c) $I_{ac} = 1.5$ mA. Solid black lines fit to Eq. (2). Data offset in y -axis for clarity. **d** Hollow

squares represent the amplitude of $\cos \phi$ components of $V_{xy}^{2\omega}$ in Eq. (3). Dotted lines are fits for the linear, thermal contribution to $V_{xy}^{2\omega}$ from ordinary Nernst effect and spin Seebeck effect. **e** Anti-damping-like field contribution to $V_{xy}^{2\omega}$ (solid squares) and their theoretical fit, with $H_k = 38$ kOe. Inset: ΔH_{DL} extracted for the two current level, and their fitting line, with near zero y -intercept. Error bars represent a 95% confidence interval. Measurements taken at 300 K.

SOT-induced components and can lead to overestimation of SOT efficiency unless systematically eliminated from $V_{xy}^{2\omega}$ ³⁴. Joule heating in the device, proportional to I_{ac}^2 (and hence containing 2ω component), creates a vertical thermal gradient. The voltage measured along the y -axis, is thus proportional to the component of H_{ext} along x -axis through the ordinary Nernst effect (ONE)³⁵ and to M_x through the anomalous Nernst effect (ANE) and spin-Seebeck effect (SSE). As a result, the SHH voltage takes the form³⁵,

$$V_{xy}^{2\omega} = P \cos \phi + Q \cos(2\phi) \cos \phi \quad (2)$$

where,

$$P = \frac{I_{ac} R_{xy}^{AHE}}{2} \frac{\Delta H_{DL}}{H_{ext} - H_k} + V_{xy}^{ONE} H_{ext} + V_{xy}^{SSE} \quad (3)$$

$$Q = I_{ac} R_{xy}^{PHE} \frac{\Delta H_{FL} + H_{Oe}}{H_{ext}} \quad (4)$$

Here, ΔH_{DL} , ΔH_{FL} and H_{Oe} are the effective fields corresponding to current induced anti-damping-like (ADL) torque, field-like torque and Oersted field, respectively. $H_k = 38$ kOe is the effective anisotropy field, V_{xy}^{ONE} is the SHH voltage per unit applied field and V_{xy}^{SSE} is the field-independent SSE and ANE contribution.

The SHH voltage corresponding to AC excitation of amplitude 1 mA and 1.5 mA in device D1 is plotted in Figs. 4b and 4c, respectively. The solid black lines correspond to least squared error fit of the recorded voltage to Eq. (2). The $\cos \phi$ components of the voltages,

corresponding to combined ADL torque, ONE and SSE/ANE contribution, is plotted against H_{ext} in Fig. 4d. As can be noted from Eq. (3), the ADL component dwindles upon increasing H_{ext} far over H_k and we expect to see a linear scaling of $V_{xy}^{2\omega}$ at high fields due to the dominant ONE and SSE/ANE. Thus, a linear fit to $V_{xy}^{2\omega}$ at high fields (dotted lines in Fig. 4d) can be used to eliminate thermal contributions from the SHH voltage. Figure 4e shows the SHH voltage corresponding solely to ADL torque, obtained upon subtraction of thermal contributions from $V_{xy}^{2\omega}$ in Fig. 4d. We estimate an anti-damping-like field per unit current density of $\frac{\Delta H_{DL}}{J_c} = 1.34 \times 10^{-10}$ Oe A⁻¹ m², where J_c is the current density in Pt only, calculated based on the parallel resistor model (Supplementary Information Section 1). The anti-damping-like spin torque efficiency can then be calculated as,

$$\xi_{DL} = \left(\frac{2e}{\hbar} \right) M_s t_{FM} \frac{\mu_0 \Delta H_{DL}}{J_c} \quad (5)$$

Using the bulk saturation magnetization of our FGaT crystals, $M_s = 5.8$ emu g⁻¹ (or 3.95×10^4 A m⁻¹), we obtain $\xi_{DL} = 0.093$ for our FGaT/Pt device. Similar measurements in device D2 resulted in $\xi_{DL} = 0.098$ as presented in Supplementary Fig. 5. These values are in good agreement with that expected from a SOT system using Pt as the spin-Hall material with a metallic ferromagnet³⁶. We also provide a comparison of threshold switching current density, ADL torque per unit current and SOT efficiency from various previous reports of deterministic magnetization switching in vdW magnetic materials in Supplementary Information Section 3.

Discussion

We have demonstrated current-induced, deterministic switching (type-z) of out-of-plane magnetization in a $\text{Fe}_3\text{GaTe}_2/\text{Pt}$ bilayer spin-orbit torque system up to 320 K, with a low switching current density of $1.69 \times 10^6 \text{ A cm}^{-2}$ at room temperature. Furthermore, using second harmonic Hall voltage measurements, we have quantitatively estimated the effective anti-damping-like field and spin-torque efficiency of the FGaT/Pt system, and found it to be in good agreement with previous reports of Pt-based SOT systems. Our FGaT/Pt devices not only works beyond room temperature but also achieves switching at one of the lowest current densities (barring the CGT/Pt system³⁷, where the FM is an insulator and hence not suitable for magnetic tunnel junctions) providing an energy efficient alternative for spintronic devices. While the ADL SOT efficiency for our FGaT/Pt devices (≈ 0.1) is close to the commonly observed bulk ferromagnet/Pt systems, the observed switching current density is almost an order of magnitude smaller. This may be attributed to the possible existence of a current-based control of magnetic anisotropy in FGaT, as has been observed in its close analogue, Fe_3GeTe_2 ^{38–40}. The existence and extent of this effect in FGaT, however, remains to be explored. During the preparation of this manuscript, we came across an archived report by Li et al. on a similar system of FGaT/Pt⁴¹. We would like to note that the threshold switching current density we report is almost an order of magnitude smaller than that of Li et al. Furthermore, while their reported $\xi_{\text{DL}} = 0.22$ is larger, it may be attributed to oversight of thermal contributions to the SHH voltage even upon operating at current densities larger than ours, as has been argued previously³⁷ to result in overestimation of SOT effects¹⁸. By fully accounting for these contributions, we assume that our SOT efficiency value, although smaller, might be a more representative estimate for the FGaT/Pt bilayer system. This work marks an important step in the adoption of vdW magnetic materials for building spintronic devices for non-volatile, energy-efficient memories and computing devices.

Methods

Bulk crystal growth and characterization

Single crystals of Fe_3GaTe_2 were synthesized through a Te self-flux method as described by Zhang et al.²³. A mixture of Fe powder (Beantown Chemical, 99.9%), Ga ingot (Alfa Aesar, 99.99999%), and Te pieces (Sigma Aldrich, 99.999%) were weighed in a molar ratio of 1:2:2 in a nitrogen-filled glovebox (with H_2O and O_2 levels less than 0.1 ppm) and placed in an alumina Canfield crucible. The mixture-filled crucible was flame-sealed in an evacuated quartz tube with quartz wool and subsequently heated to 1000 °C from room temperature within an hour. The mixture dwelled for 24 h and subsequently cooled to 880 °C within an hour followed by a slow cooling to 780 °C at a rate of 1 °C per hour. Centrifugation was performed to remove the excess flux and afterwards the products were heat-treated to alleviate the concentration of tellurium defects. The resulting products contain a mixture of products with a silver luster among which contain Fe_3GaTe_2 crystals which are millimeter sized.

Powder X-ray diffraction (PXRD) data were measured on bulk samples using an X'Pert Pro diffractometer (PANalytical) in Bragg-Brentano geometry operating with a curved Ge(III) monochromator and $\text{Cu K}\alpha$ radiation with a wavelength of 0.154 nm. Scanning electron microscope (SEM) images on both bulk crystals and exfoliated flakes on SiO_2 substrates are measured using a Zeiss Merlin high-resolution SEM system with images acquired at an acceleration voltage of 20 kV, a current of 1000 pA, and a working distance of 8.5 mm. SEM-energy dispersive X-ray spectroscopy (EDS) elemental maps were taken using the EDAX APEX software.

Electrical transport measurements were performed on the bulk crystals in a Physical Property Measurement System (PPMS Dynacool, Quantum Design) in a five-probe geometry with contacts made of silver epoxy H20E and platinum wires. Direct current magnetization of

the sample was acquired using the Vibrating Sample Magnetometer (VSM) option on crystals placed in the proper orientation using Kapton tape on a quartz holder (OOP) or using a Brass holder (IP). Temperature-dependent field-cooled and zero-field-cooled magnetization measurements were performed with an applied magnetic field of 1000 Oe. Specific heat capacity was measured on a 4.4 mg crystal using the Heat Capacity (HC) option with Apiezon H vacuum grease applied on the platform.

Device fabrication

Fe_3GaTe_2 flakes were exfoliated on Si/SiO_2 dies in a nitrogen-filled glovebox. For FGaT/Pt devices, the dies after exfoliation were sealed in the glovebox and only briefly exposed to air while transferring to the load-lock chamber of the sputterer. An RF plasma cleaning step was performed, under 4 mTorr Ar pressure and 40 W for 15 s, to remove any nascent oxide from FGaT surface. Subsequently, 6 nm Pt was deposited at a rate of 1.8 A s^{-1} . 6-terminal Hall bars were patterned into the FGaT/Pt stack through e-beam lithography using negative resist ma-N2403, followed by Ar ion-milling (300 keV, 300 s, 70° inclination). Finally, lift-off through photolithography was used to pattern contact traces and pads for the etched Hall bars. Ti/Au (5 nm/70 nm) was e-beam deposited to create these metallic contacts. FGaT-only devices for magneto-transport characterization were fabricated using e-beam lithography with PMMA resist and Ti/Au (5 nm/35 nm) contacts, ensuring under a minute of direct exposure of FGaT flakes to ambient air. These devices were additionally encapsulated with thick hBN flakes in a glovebox using PDMS-based dry transfer.

Transport measurements

All transport measurements were performed in a 9 T PPMS DynaCool system. Anomalous Hall effect measurements on the FGaT-only devices were performed using the Electrical Transport Option of the PPMS Dynacool, with a drive current of 100 μA . Current-induced switching experiments were performed by interfacing a Keithley 6221 current source and 2182A nanovoltmeter with the PPMS Dynacool. Current input sequence consisted of a 1 ms write-pulse followed by 999 ms of read pulses ($\pm 200 \mu\text{A}$). For second harmonic Hall measurements, AC current was supplied by the Keithley 6221, at a frequency 1711.97 Hz. Two lock-in amplifiers, Stanford Research Systems (SRS) SR860 were used to simultaneously measure f and $2f$ transverse voltage components.

Data availability

Source data are available in the Dryad repository⁴², <https://doi.org/10.5061/dryad.lrn8pk11k>.

References

1. Hirohata, A. et al. Review on spintronics: principles and device applications. *J. Magn. Magn. Mater.* **509**, 166711 (2020).
2. Fong, X. et al. Spin-transfer torque devices for logic and memory: prospects and perspectives. *IEEE Trans. Comput. Des. Integr. Circuits Syst.* **35**, 1–22 (2016).
3. Ohno, H., Stiles, M. D. & Dieny, B. Spintronics. *Proc. IEEE* **104**, 1782–1786 (2016).
4. Grollier, J. et al. Neuromorphic spintronics. *Nat. Electron.* **3**, 360–370 (2020).
5. Kaiser, J. & Datta, S. Probabilistic computing with p-bits. *Appl. Phys. Lett.* **119**, 150503 (2021).
6. Camsari, K. Y., Sutton, B. M. & Datta, S. P-bits for probabilistic spin logic. *Appl. Phys. Rev.* **6**, 011305 (2019).
7. Safranski, C. et al. Reliable sub-nanosecond switching in magnetic tunnel junctions for MRAM applications. *IEEE Trans. Electron Dev.* **69**, 7180–7183 (2022).
8. Safranski, C. et al. Demonstration of nanosecond operation in stochastic magnetic tunnel junctions. *Nano Lett.* **21**, 2040–2045 (2021).

9. Gajek, M. et al. Spin torque switching of 20 nm magnetic tunnel junctions with perpendicular anisotropy. *Appl. Phys. Lett.* **100**, 132408 (2012).
10. Gong, C. et al. Discovery of intrinsic ferromagnetism in two-dimensional van der Waals crystals. *Nature* **546**, 265–269 (2017).
11. Huang, B. et al. Layer-dependent ferromagnetism in a van der Waals crystal down to the monolayer limit. *Nature* **546**, 270–273 (2017).
12. Fei, Z. et al. Two-dimensional itinerant ferromagnetism in atomically thin Fe₃GeTe₂. *Nat. Mater.* **17**, 778–782 (2018).
13. Samarth, N. Magnetism in flatland. *Nature* **546**, 216–217 (2017).
14. Kajale, S. N. et al. Two-dimensional magnetic materials for spintronic applications. *Nano Res.* <https://doi.org/10.1007/s12274-024-6447-2> (2024).
15. Seo, J. et al. Nearly room temperature ferromagnetism in a magnetic metal-rich van der Waals metal. *Sci. Adv.* **6**, eaay8912 (2020).
16. May, A. F. et al. Ferromagnetism near room temperature in the cleavable van der Waals crystal Fe₅GeTe₂. *ACS Nano* **13**, 4436–4442 (2019).
17. Alghamdi, M. et al. Highly efficient spin-orbit torque and switching of layered ferromagnet Fe₃GeTe₂. *Nano Lett.* **19**, 4400–4405 (2019).
18. Wang, X. et al. Current-driven magnetization switching in a van der Waals ferromagnet Fe₃GeTe₂. *Sci. Adv.* **5**, 2–8 (2019).
19. Fujimura, R. et al. Current-induced magnetization switching at charge-transferred interface between topological insulator (Bi,Sb)2Te₃ and van der Waals ferromagnet Fe₃GeTe₂. *Appl. Phys. Lett.* **119**, 1–4 (2021).
20. Kao, I. H. et al. Deterministic switching of a perpendicularly polarized magnet using unconventional spin-orbit torques in WTe₂. *Nat. Mater.* **21**, 1029–1034 (2022).
21. Shin, I. et al. Spin-orbit torque switching in an all-Van der Waals heterostructure. *Adv. Mater.* **34**, 1–7 (2022).
22. Wang, L. et al. Cascadable in-memory computing based on symmetric writing and readout. *Sci. Adv.* **8**, 1–11 (2022).
23. Zhang, G. et al. Above-room-temperature strong intrinsic ferromagnetism in 2D van der Waals Fe₃GaTe₂ with large perpendicular magnetic anisotropy. *Nat. Commun.* **13**, 1–8 (2022).
24. Zhu, W. et al. Large room-temperature magnetoresistance in van der Waals ferromagnet/semiconductor junctions. *Chin. Phys. Lett.* **39**, 128501 (2022).
25. Yin, H. et al. Fe₃GaTe₂/MoSe₂ ferromagnet/semiconductor 2D van der Waals heterojunction for room-temperature spin-valve devices. *CrystEngComm* **25**, 1339–1346 (2023).
26. Jin, W. et al. Room-temperature spin-valve devices based on Fe₃GaTe₂/MoS₂/Fe₃GaTe₂ 2D van der Waals heterojunctions. *Nanoscale* **15**, 5371–5378 (2023).
27. Jin, W. et al. Room-temperature and tunable tunneling magnetoresistance in Fe₃GaTe₂-Based 2D van der Waals heterojunctions. *ACS Appl. Mater. Interfaces* **15**, 36519–36526 (2023).
28. Fukami, S., Anekawa, T., Zhang, C. & Ohno, H. A spin-orbit torque switching scheme with collinear magnetic easy axis and current configuration. *Nat. Nanotechnol.* **11**, 621–625 (2016).
29. Liu, Y. T. et al. Anatomy of type-*x* spin-orbit-torque switching. *Phys. Rev. Appl.* **16**, 1 (2021).
30. Tan, C. et al. Hard magnetic properties in nanoflake van der Waals Fe₃GeTe₂. *Nat. Commun.* **9**, 1–7 (2018).
31. Liu, L., Lee, O. J., Gudmundsen, T. J., Ralph, D. C. & Buhrman, R. A. Current-induced switching of perpendicularly magnetized magnetic layers using spin torque from the spin hall effect. *Phys. Rev. Lett.* **109**, 1–5 (2012).
32. Garello, K. et al. Symmetry and magnitude of spin-orbit torques in ferromagnetic heterostructures. *Nat. Nanotechnol.* **8**, 587–593 (2013).
33. Hayashi, M., Kim, J., Yamanouchi, M. & Ohno, H. Quantitative characterization of the spin-orbit torque using harmonic Hall voltage measurements. *Phys. Rev. B Condens. Matter Mater. Phys.* **89**, 1–15 (2014).
34. Avci, C. O. et al. Interplay of spin-orbit torque and thermoelectric effects in ferromagnet/normal-metal bilayers. *Phys. Rev. B - Condens. Matter Mater. Phys.* **90**, 1–11 (2014).
35. Roschewsky, N. et al. Spin-orbit torque and Nernst effect in Bi-Sb/Co heterostructures. *Phys. Rev. B* **99**, 1–5 (2019).
36. Zhu, L., Ralph, D. C. & Buhrman, R. A. Maximizing spin-orbit torque generated by the spin Hall effect of Pt. *APL Mater.* **8**, 031308 (2021).
37. Gupta, V. et al. Manipulation of the van der Waals magnet Cr₂Ge₂Te₆ by spin-orbit torques. *Nano Lett.* **20**, 7482–7488 (2020).
38. Johansen, Ø., Risinggård, V., Sudbø, A., Linder, J. & Brataas, A. Current control of magnetism in two-dimensional Fe₃GeTe₂. *Phys. Rev. Lett.* **122**, 1–6 (2019).
39. Zhang, K. et al. Gigantic current control of coercive field and magnetic memory based on nanometer-thin ferromagnetic van der Waals Fe₃GeTe₂. *Adv. Mater.* **33**, 1–8 (2021).
40. Zhang, K. et al. Highly efficient nonvolatile magnetization switching and multi-level states by current in single Van der Waals topological ferromagnet Fe₃GeTe₂. *Adv. Funct. Mater.* **31**, 2105992 (2021).
41. Li, W. et al. Room-temperature van der Waals 2D ferromagnet switching by spin-orbit torques. *arXiv* **2304.10718**, (2023).
42. Kajale, S. Current-induced switching of a van der Waals ferromagnet at room temperature [Dataset]. *Dryad* <https://doi.org/10.5061/dryad.1rn8pk1k> (2024).

Acknowledgements

This work was carried out in part through the use of MIT.Nano’s facilities. This work was performed in part at the Harvard University Center for Nanoscale Systems (CNS); a member of the National Nanotechnology Coordinated Infrastructure Network (NNCI).

Author contributions

S.N.K. and T.N. contributed equally to this work. S.N.K. and D.S. designed the project. T.N., A.B. and M.L. grew the bulk FGaT crystals. T.N., M.L., and C.A.C. characterized the bulk FGaT crystals. S.N.K. fabricated the devices and performed the experiments with assistance from D.S., T.N., M.L., and D.C.B. S.N.K., T.N., and D.S. wrote the manuscript with contributions from all authors.

Competing interests

The authors declare no competing interests.

Additional information

Supplementary information The online version contains supplementary material available at <https://doi.org/10.1038/s41467-024-45586-4>.

Correspondence and requests for materials should be addressed to Deblina Sarkar.

Peer review information *Nature Communications* thanks Xuanyao Fong, and the other, anonymous, reviewer(s) for their contribution to the peer review of this work. A peer review file is available.

Reprints and permissions information is available at <http://www.nature.com/reprints>

Publisher’s note Springer Nature remains neutral with regard to jurisdictional claims in published maps and institutional affiliations.

Open Access This article is licensed under a Creative Commons Attribution 4.0 International License, which permits use, sharing, adaptation, distribution and reproduction in any medium or format, as long as you give appropriate credit to the original author(s) and the source, provide a link to the Creative Commons licence, and indicate if changes were made. The images or other third party material in this article are included in the article's Creative Commons licence, unless indicated otherwise in a credit line to the material. If material is not included in the article's Creative Commons licence and your intended use is not permitted by statutory regulation or exceeds the permitted use, you will need to obtain permission directly from the copyright holder. To view a copy of this licence, visit <http://creativecommons.org/licenses/by/4.0/>.

© The Author(s) 2024